catalysts

MDPI

Article

Fe-N-C Catalyst Derived from MOFs with Enhanced Catalytic Performance for Selective Oxidation of Emerging Contaminants

Cheng Zeng [1], Yan Wang [1,2,*], Jinquan Wan [1,2] and Zhicheng Yan [1]

[1] College of Environment and Energy, South China University of Technology, Guangzhou 510006, China
[2] Guangdong Plant Fiber High-Valued Cleaning Utilization Engineering Technology Research Center, Guangzhou 510006, China
* Correspondence: yanwang@scut.edu.cn

Abstract: Fe-N-C/peroxymonosulfate (PMS) systems have demonstrated selective oxidation of pollutants, but the underlying mechanism and reasons for variability remain unclear. In this work, we synthesized a highly active Fe-N-C catalyst derived from MOFs using a pyrolysis protection strategy. We assessed its catalytic activity by employing PMS as an activator for pollutant degradation. The presence of Fe-Nx sites favored the catalytic performance of FeMIL-N-C, exhibiting 23 times higher activity compared to N-C. Moreover, we investigated the degradation performance and mechanism of the FeMIL-N-C/PMS system through both experimental and theoretical analyses, focusing on pollutants with diverse electronic structures, namely bisphenol A (BPA) and atrazine (ATZ)N-C. Our findings revealed that the degradation of ATZ primarily follows the free radical pathway, whereas BPA degradation is dominated by electron transfer pathways. Specifically, pollutants with a low LUMO- HOMO energy gap (BPA) can be degraded via the FeMIL-N-C/PMS system through the electron transfer pathway. Conversely, pollutants with a high LUMO-HOMO energy gap (ATZ) exhibit limited electron donation and predominantly undergo degradation through the free radical pathway. This work introduces novel insights into the mechanisms underlying the selective oxidation of pollutants, facilitating a deeper understanding of effective pollutant removal strategies.

Keywords: Fe-N-C catalyst; peroxymonosulfate; electronic transfer; radical

Citation: Zeng, C.; Wang, Y.; Wan, J.; Yan, Z. Fe-N-C Catalyst Derived from MOFs with Enhanced Catalytic Performance for Selective Oxidation of Emerging Contaminants. *Catalysts* **2023**, *13*, 1021. https://doi.org/10.3390/catal13061021

Academic Editors: Shaohong Zang and Liuye Mo

Received: 2 May 2023
Revised: 8 June 2023
Accepted: 9 June 2023
Published: 19 June 2023

1. Introduction

Over the past decade, the consumption of emerging contaminants (ECs) such as pharmaceuticals and personal care products, pesticides, antibiotics, and other substances has increased significantly. These ECs are frequently detected in natural wastewater and industrial effluents [1]. However, once they enter the aquatic environment, these contaminants become challenging to remove and pose a significant risk to aquatic organisms and ecosystems [2,3]. Consequently, the development of safe and effective treatment methods for ECs is of paramount importance in the field of environmental remediation [4–6].

Advanced oxidation processes (AOPs) based on persulfate (peroxydisulfate and peroxymonosulfate) have gained significant attention in the field of degradation of ECs [7,8]. These processes are favored due to the high oxidation potential, chemical stability, and wide pH applicability of persulfate [9–11]. PDS and PMS have been presented as the most potent oxidants for environmental remediation in various studies [12]. However, at room temperature, both PDS and PMS exhibit relatively stable and limited oxidation capacity, as they are not readily decomposed spontaneously [13]. To achieve the rapid removal of ECs, it is crucial to catalytically activate persulfates under specific conditions [14–17], promoting the gradual decomposition and generation of various reactive oxygen species (sulfate radicals, hydroxyl radicals, singlet oxygen, etc.) with a strong oxidizing ability [18–20]. This activation approach enables the efficient degradation of ECs.

Among the various methods for activating persulfates, transition metal activation has proven to be the most effective and commonly employed method [21]. Both homogeneous Fe^{2+} and heterogeneous Fe catalysts are the most promising applications due to the environmental friendliness of ions [22–24]. However, homogeneous Fe^{2+} suffers from issues such as the formation of secondary contamination, while heterogeneous Fe materials usually exhibit low atomic utilization and low efficiency [25]. In contrast, Fe-N-C catalysts are heterogeneous catalytic materials characterized by low leaching of metal ions and high catalytic efficiency. The presence of nitrogen (N) allows for coordination with Fe atoms, forming Fe-Nx catalytic sites that reduce adsorption energy and enhance catalytic efficiency [26–28]. Nonetheless, conventional Fe-N/C catalysts tend to aggregate Fe nanoparticles during preparation, leading to decreased atomic utilization, dispersion, and density of Fe-Nx, which negatively impacts catalytic activity. Moreover, the conventional Fe-N/C catalysts are prone to leaching iron ions when used in highly acidic environments, leading to secondary contamination.

In addition, several reaction mechanisms have been proposed in the available literature, highlighting that the degradation pathways of pollutants may be influenced not only by the catalysts but also by the properties of the pollutants themselves [29–32]. For example, Xu et al. synthesized a single-atom catalyst FeSA-CN with an Fe-N_4 active site for PMS activation by encapsulating iron acetylacetonate ($Fe(acac)_3$) inside ZIF-8 [6]. They found that Fe-N_4, graphite N, and pyridine N could all serve as adsorption sites for SSZs. Fe-N_4 was capable of adsorbing two PMS molecules, activating them into two Fe-N_4 able to adsorb two PMS molecules, activating them into two PMS anion radicals (SO_5^-), and further self-assembling to generate singlet oxygen ($^1O_2$) and $S_2O_8^{2-}$. This cascade of reactions facilitated the degradation mechanism of persulfate with $^1O_2$ as the main reactive oxygen, along with hydroxyl radicals (·OH) and sulfate radicals (SO_4^-). Similarly, Hu proposed that Fe atoms in Fe-N_4 could transfer electrons to PMS, resulting in the production of ·OH and SO_4^-. The C atom linked to pyridine N converts PMS to SO_5^- and further to $^1O_2$ by taking electrons from PMS. Both the free radical and non-free radical pathways contributed to the degradation of BPA. Despite being synthesized in different ways, these materials shared the common active structure of Fe-N4 and played a major role in the degradation process. Recently, it has been reported that the degradation of pollutants in carbon nanotube/persulfate systems is related to their own oxidation potentials [33,34]. However, there are few reports on Fe-N-C materials, so it is necessary to investigate them in depth.

In this work, we prepared a novel catalyst FeMIL-N-C with an active Fe-Nx site to activate PMS for the degradation of various pollutants. To prevent Fe agglomeration, we employed a protection-pyrolysis strategy during catalyst preparation. In addition, metal-free N-C materials without an additional Fe source were also prepared for comparison. We selected bisphenol A and atrazine as electron-rich and electron-poor pollutants, respectively, for comparative studies. We found that the FeMIL-N-C/PMS system has different removal mechanisms (radical or non-radical) for different pollutants, which are related to the LUMO-HOMO energy gap of the pollutants. This suggests that the removal mechanisms of pollutants are influenced by the intrinsic properties of the pollutants themselves, rather than solely being determined by the catalysts employed. The insights gained from this work contribute to a better understanding of how to achieve the effective removal of pollutants in environmental remediation processes.

2. Results and Discussion

2.1. Characterization of Catalysts

The catalysts' morphology was characterized using scanning electron microscopy (SEM) and transmission electron microscopy (TEM), and the results are shown in Figure 1a–f. Figure 1a shows that ZIF-8 is a surface-smooth dodecahedral rhombus with a small size, which is due to the addition of CTAB to limit its growth. Such a smaller particle size of ZIF-8 has a positive effect on limiting Fe agglomeration. The FeMIL exhibits a dodecahedral

spindle shape (Figure 1b), consistent with previous reports. Due to the effect of CTAB, ZIF-8 was able to grow crystallographically on the surface of FeMIL [8], and, finally, the FeMIL was completely coated, and FeMIL-ZIF was obtained (Figure 1c). The FeMIL- N-C material obtained after pyrolysis at 800 °C retains the intact crystal form of FeMIL, while the peripheral ZIF-8 exhibits a reduced crystal structure but still retains an intact crystal structure (Figure 1d). Conversely, the P-FeMIL material without ZIF-8 protection shows a fragmented state with a significantly disturbed crystal structure (Figure S1). This confirms that the protection pyrolysis strategy is successful as it effectively protects the inner FeMIL layer, preserving the intact crystal structure and ensuring the uniform distribution of Fe (Figure 1e,f). It is worth noting that the EDX image of FeMIL-ZIF shows the presence of Zn (Figure S2), while no Zn is observed on the EDX image of FeMIL-N-C. This suggests that the element Zn has volatilized during high-temperature pyrolysis, so the original Zn-N_4 coordination forms an N defect that facilitates the incorporation of Fe atoms and the formation of Fe-Nx catalytic sites.

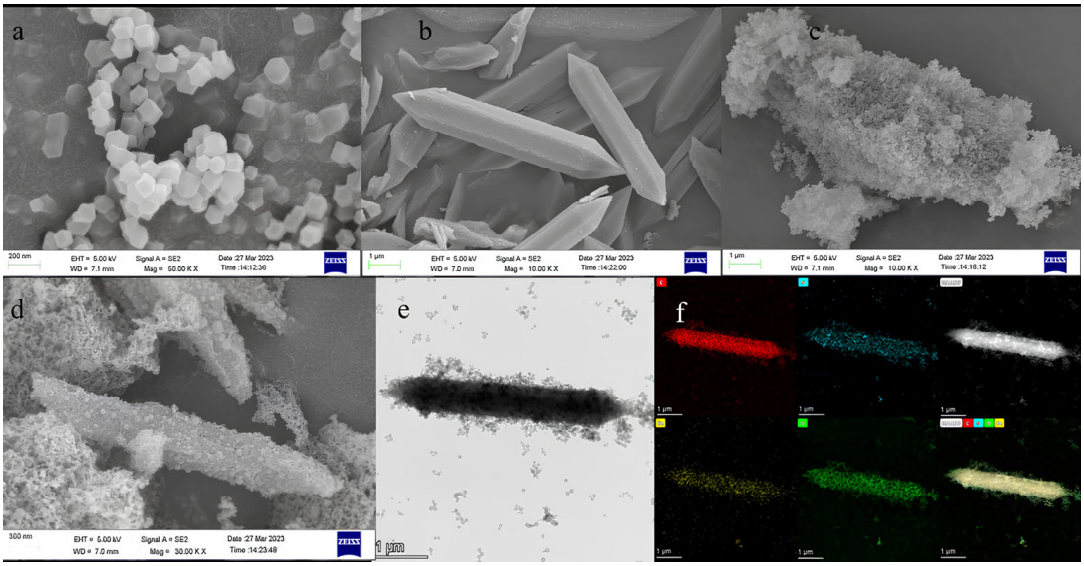

Figure 1. (**a**) SEM image of (**a**) ZIF-8, (**b**) FeMIL, (**c**) FeMIL-ZIF, (**d**) FeMIL-N-C, and (**e**) TEM image of FeMIL-N-C and (**f**) corresponding EDX mapping images, C (red), N (blue), Fe (yellow), O (green).

The crystal structure of the catalyst was examined by XRD, and the results are shown in Figure 2a. FeMIL-N-C showed only two characteristic peaks corresponding to graphitic carbon, and no characteristic peaks of Fe were observed. This proves that Fe did not aggregate into nanoparticles during the pyrolysis process [35,36]. This further supports the effectiveness of the protected pyrolysis strategy in preventing metal agglomeration and improving catalytic activity, as metal agglomeration during pyrolysis is known to inhibit catalytic performance. The functional group species in the catalyst were identified using Fourier-transform infrared spectroscopy (FT-IR), as shown in Figure 2b. The coordination structure of Fe-Nx is favored due to the Fe in Fe(MIL) coordinates with the phenyl group and binds more readily to the π-π bond of the ZIF-8 ligand. The peaks at 1500–1380 cm^{-1} in ZIF-8 originated from C–N stretching vibrations in the heteroaromatic ring, and the peak at 1585 cm^{-1} was attributed to C=N vibrations. In Fe(MIL), the peaks at 1550–1420 cm^{-1} were attributed to aromatic ring vibrations, and the peaks at 1320–1820 cm^{-1} were attributed to C–H vibrations in the aromatic plane. This suggests that the phenyl structure in Fe(MIL) forms π-π interactions with the ZIF-8 ligand, enhancing the susceptibility to N capture and promoting the formation of Fe-Nx sites. The specific surface area and pore size distribution of the three post-pyrolysis materials were analyzed using N_2 adsorption–desorption isotherm curves, as shown in Figure 2c,d. FeMIL-N-C, N–C, and P-FeMIL are all IV-type curves with H3 hysteresis loops. The large specific surface area of FeMIL-N-C is attributed to the pyrolysis of the outer layer of attached ZIF-8, which produces a rich

pore structure. This indicates that all three pyrolyzed materials have abundant micropore-mesopore coexistence structures, and N–C and FeMIL-N-C materials also have mesopores with pore sizes around 25 nm, while P-FeMIL, which is pyrolyzed alone, has none. This 25 nm pore is generated by the pyrolysis of ZIF-8, and many ZIF-8 is attached to the surface of FeMIL-N-C, while there is no ZIF-8 on the surface of P-FeMIL. The larger pore size and coexistence of micropores and mesopores would be beneficial to improve the mass transfer efficiency of the catalyst with PS and contaminants.

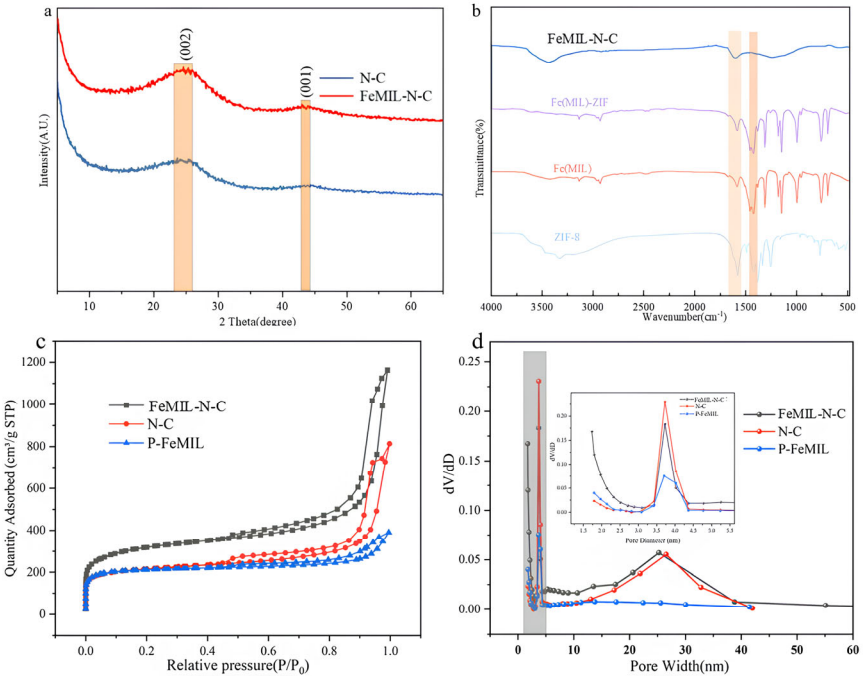

Figure 2. (**a**) XRD pattern of N-C and FeMIL-N-C, (**b**) FT-IR, (**c**) nitrogen adsorption and desorption curves of three pyrolysis materials, and (**d**) pore size distribution.

The X-ray photoelectron spectroscopy (XPS) survey spectrum of FeMIL-N-C revealed the presence of four main elements: Fe, C, N, and O, with no detectable Zn element, and no Zn element was detected (Figure 3). This confirms the complete volatilization of Zn, thus favoring the formation of Fe-Nx sites. The XPS C 1s spectrum of FeMIL-N-C exhibited three peaks corresponding to C–C (284.5 eV), C–O/C–N (285.6 eV), and O–C=O (288.1 eV) [32,37,38]. Moreover, the N1s fine spectrum displayed five components: Pyridine N (398.2 eV), Fe-N (399.1 eV), pyrroline N (400.6 eV), graphite N (401.3 eV), and oxidized N (404.0 eV) [39,40]. The respective contents are given in Figure S2, which contains 19.3% pyridine N and 18.2% graphite N. Previous studies have highlighted that pyridine N is the N species coordinated to Fe and can also act as an active site contributing electrons to activate the neighboring carbon atoms, whereupon the active carbon atoms are converted to Lewis bases, increasing the adsorption capacity of the catalyst for impurities. Raman mapping of FeMIL-N-C and N–C showed a D band at 1360 cm^{-1} and a G band at 1582 cm^{-1}. The D band represents amorphous and defect structures on the surface of carbon materials, typically attributed to the vibration of sp^3 hybridized C atoms, indicating the defect level of graphitic carbon. Conversely, the G band corresponds to the characteristic peak of crystalline carbon, arising from the stretching vibration of the sp^2 hybridized structure of C atoms [29,41]. Normally, I_D/I_G can indicate the defect level of the material, and a larger value means a higher defect level. The defect level of FeMIL-N-C is slightly lower than that of metal-free N-C (1.08 vs. 1.19), which may be due to the coordination of Fe atoms and defective N sites to form Fe-N. Based on the above results, we can confirm that the pyrolysis protection strategy successfully prevented Fe agglomeration and formed Fe-N-C catalysts derived from MOFs with Fe-Nx catalytic sites.

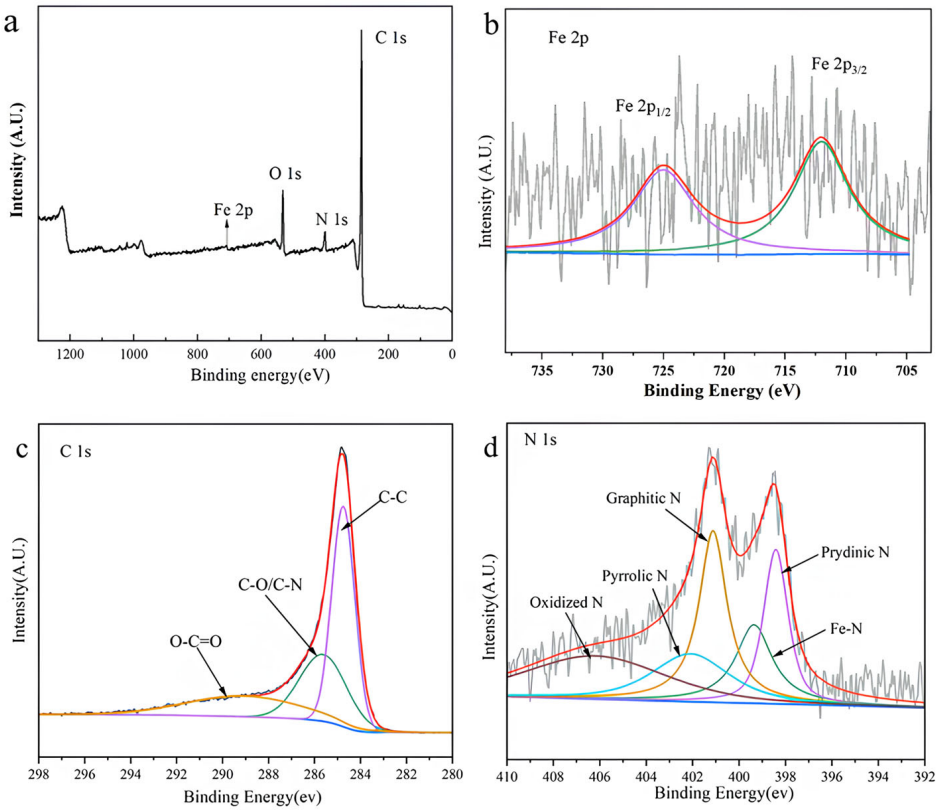

Figure 3. XPS images of FeMIL-N-C: (**a**) Survey, (**b**) Fe 2p, (**c**) C 1s, (**d**) N 1s.

2.2. Catalytic Oxidation of Different Pollutants in the FeMIL-N-C/PMS System

The catalytic performance of FeMIL-N-C with Fe-Nx sites was evaluated by activating PMS for the degradation of different pollutants. As shown in Figure 4a,b, SMX, BPA, and CIP were completely removed by the FeMIL-N-C/PMS system within 20 min, with BPA being completely removed within 10 min. However, the degradation of MNZ, TCP, and ATZ in the FeMIL-N-C/PMS system was not significant. Less than 40% of ATZ was removed within 60 min, and less than 50% of MNZ and TCP were removed. The corresponding rate constants (k value) were only 0.022 min^{-1}, 0.019 min^{-1}, and 0.013 min^{-1}, respectively. In comparison, the k value of BPA was as high as 0.66 min^{-1}. The k value of BPA was higher than that of the FeMIL-N-C/PMS system.

Similarly, the N-C/PMS system exhibited a comparable trend, albeit with lower removal rates and k values compared to the FeMIL-N-C/PMS system with Fe-Nx sites. These results indicate two important findings. Firstly, FeMIL-N-C exhibits excellent catalytic activity, with up to 23 times the catalytic activity of the metal-free N-C material under the same conditions. Secondly, FeMIL-N-C and N-C materials have similar degradation patterns for different pollutants, confirming the selective oxidation ability of FeMIL-N-C towards diverse pollutants. To further investigate where the differences in the degradation mechanisms of different pollutants are, BPA and ATZ were selected as targets for further investigation because BPA and ATZ showed very different degradation rates in the degradation experiments [42].

Initially, degradation experiments were conducted for BPA and ATZ under varying PMS dosages and different catalyst dosages to determine the optimized reaction conditions. Figure S3 demonstrates that in the FeMIL-N-C/PMS/BPA system, the effect of PMS dosage on the degradation of BPA was very limited. Even at a low PMS addition, the PMS concentration was sufficient to complete the degradation of BPA, so the continued addition of BPA could not further affect its degradation. In the FeMIL-N-C/PMS/ATZ system, however, the PMS dosage had a significant effect. As the PMS dosage increased from 0.1g·L^{-1} to 0.8g·L^{-1}, the complete degradation of ATZ was achieved within 20 min [42–44].

In contrast, the effect of FeMIL-N-C on both ATZ and BPA was not as great as the effect of PMS dosage on ATZ degradation (Figure S4). This indicates that the degradation of ATZ in the FeMIL-N-C/PMS system was more influenced by the PMS dosage, and the degradation effect was enhanced with the increase in the PMS dosage.

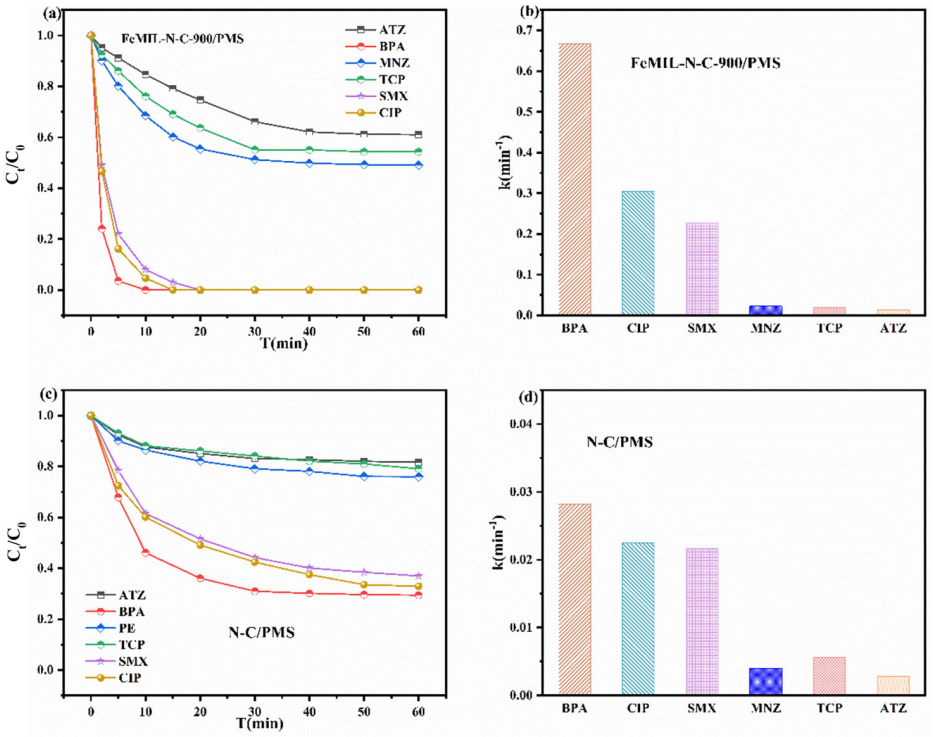

Figure 4. (**a**) Degradation of different contaminants by FeMIL-N-C/PMS system; (**b**) k_{obs} for different contaminants in the FeMIL-N-C/PMS system; (**c**) degradation of different contaminants by N-C/PMS system; (**d**) k_{obs} for different contaminants in the N-C/PMS system. Reaction conditions: [Catalyst] = 0.1 g·L^{-1}, [Contaminants] = 20 mg·L^{-1}, [PMS] = 0.3 g·L^{-1}, [V] = 100 mL, [T] = 298K.

2.3. ROS Determination

To investigate the selective oxidation ability of the FeMIL-N-C/PMS system towards different contaminants, quenching experiments were conducted to identify the reactive oxygen species (ROS) in the degradation of BPA and ATZ. Figure 4 presents the results of these experiments, where methanol (MeOH), tert-butyl alcohol (TBA), benzoquinone (BQ), and Furfuryl alcohol (FFA) were used as quenching agents for $SO_4^{\cdot-}$, OH, and O_2^{2-},$^1O_2$, respectively [41,45–47]. As shown in Figure 4a, the addition of EtOH significantly inhibited the degradation of ATZ, and similarly, TBA was able to cause the inhibition of ATZ degradation to a greater extent. Although BQ and FFA could affect the degradation rate of ATZ to some extent, they were very weak, and ATZ was still largely removed after approximately 30 min. Thus, the free radical species, especially $SO_4^{\cdot-}$, contribute significantly to the degradation of ATZ, and the degradation of ATZ is typical of free radical domination [48]. Electron paramagnetic resonance (EPR) was employed for the qualitative detection of ROS as it enables one to capture the corresponding ROS. As shown in Figure 4b, signals attributed to DMPO-·OH and DMPO- $SO_4^{\cdot-}$ were clearly observed, and the signal peaks in FeMIL-N-C/PMS/ATZ were much weaker than those in FeMIL-N-C/PMS. This decrease in signal intensity is attributed to the consumption of both radicals due to the addition of ATZ. For the FeMIL-N-C/PMS/BPA system, the addition of all four quenchers could not significantly inhibit the degradation of BPA, and the addition of FFA could cause some degree of inhibition [49], but according to the report, FFA may also cause the depletion of PMS and thus inhibit the degradation. Furthermore, this is consistent with the slight inhibition of FFA in the ATZ system, except that the inhibition of ATZ by FFA appears to be greater because ATZ is more sensitive to the PMS dosage, but whether the

effect is caused by singlet oxygen needs further verification. Moreover, EPR assays for the detection of $\cdot O_2^-$ and $^1O_2$ (Figure 5c,d) did not indicate any reduction in the signal intensity upon the addition of ATZ. Therefore, it can be indicated that $\cdot O_2^-$ and $^1O_2$ have almost no contribution to ATZ. Combining the results of the quenching experiments and EPR assays, we suggest that the degradation of ATZ is dominated by ·OH and $SO_4\cdot^-$, with $SO_4\cdot^-$ having a greater contribution, while the non-radical pathway contributes less to the degradation of ATZ.

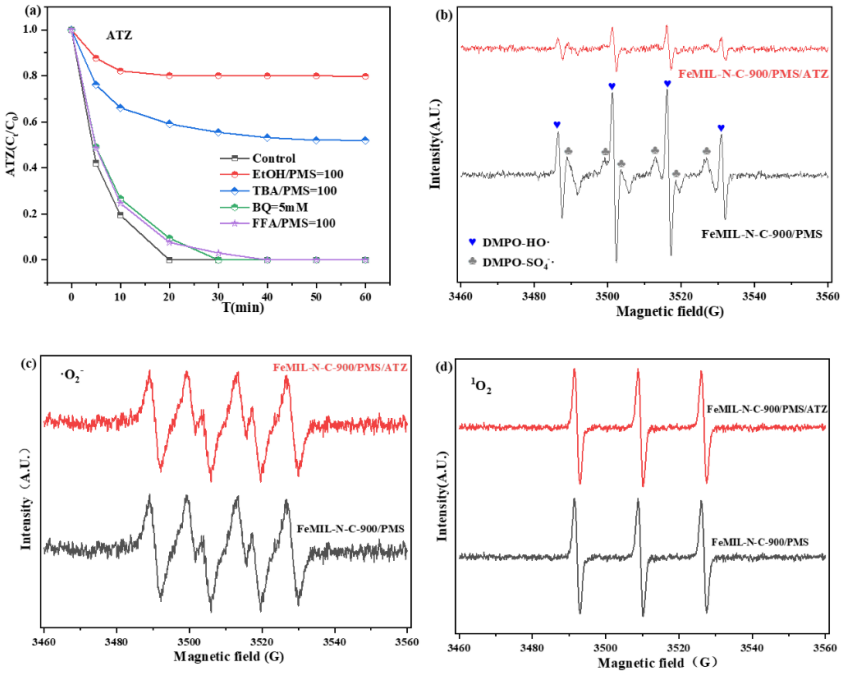

Figure 5. (**a**) Quenching experiment of ATZ degradation and EPR spectrum of (**b**) OH and SO_4^-, (**c**)·O_2^-, and (**d**) $^1O_2$. Reaction conditions: [Catalyst] = 0.1 g·L^{-1}, [Contaminants] = 20 mg·L^{-1}, [PMS] = 0.3 g·L^{-1}, [V] = 100 mL.

In the EPR assay of the FeMIL-N-C/PMS/BPA system, it was observed that the characteristic peaks of both free radicals were also present, but there was no significant difference in the intensity of the characteristic peaks in the presence or absence of contaminants. This indicates that free radical species are indeed generated in the FeMIL-N-C/PMS/BPA system, but the contribution of free radicals to the degradation of BPA is small. Therefore, it can be inferred that there is an alternative pathway that surpasses the involvement of free radicals and dominates the degradation of BPA in the FeMIL-N-C/PMS/BPA system, while in the FeMIL-N-C/PMS/ATZ system, the free radicals dominate the degradation.

In the FeMIL-N-C/PMS/BPA system, the addition of all four quenchers did not significantly inhibit the degradation of BPA (Figure 6a), with only slight inhibition observed with FFA, although it should be noted that FFA can also deplete PMS and potentially inhibit the degradation process [48]. In the EPR detection of the FeMIL-N-C/PMS/BPA system, it was found that the characteristic signal peaks attributed to ·OH and SO_4^- were also present in the FeMIL-N-C/PMS system (Figure 6c), but we found that the difference in intensity of the characteristic signal peaks obtained from the two tests in the presence or absence of BPA was not significant, which indicated that ·OH and $SO_4^-\cdot$ were also present in the FeMIL-N-C/PMS/BPA system, but contribute little to the degradation of BPA. In contrast, in the EPR test where TEMP was used as a trapping agent (Figure 6b), the FeMIL -N-C/PMS system showed a triple peak clearly attributed to $^1O_2$. This finding aligns with the results of the quenching experiments; however, the signal peak intensity of $^1O_2$ was also not significantly different in the presence or absence of BPA.

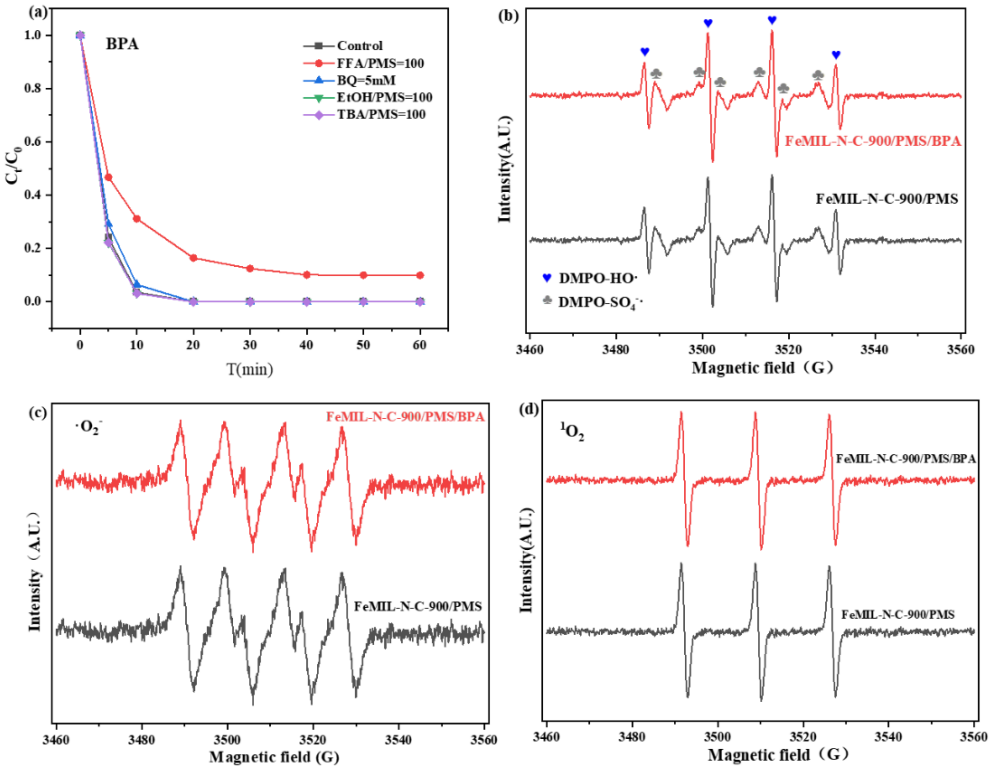

Figure 6. (**a**) Quenching experiment of BPA degradation and EPR spectrum of (**b**) ·OH and $SO_4\cdot^-$ and (**c**) $\cdot O_2^-$ and (**d**) $^1O_2$, Reaction condition: [Catalyst] = 0.1 g·L^{-1}, [Contaminants] = 20 mg·L^{-1}, [PMS] = 0.3 g·L^{-1}, [V] = 100 mL, [T] = 298 K.

2.4. Study of Degradation Mechanisms

Recent studies have indicated that BPA, which contains electron-donating groups, tends to undergo degradation through electron transfer pathways [11]. To confirm the presence of electron transfer, it is important to investigate the effect of premixed PMS and FeMIL-N-C on the degradation of contaminants. If the electron transfer pathway is dominant, premixed PMS and FeMIL-N-C should not have a significant impact on the degradation of contaminants, as the catalyst acts merely as an intermediate carrier. As shown in Figure 7a, different premixing durations of PMS and FeMIL-N-C could not inhibit the degradation of BPA, suggesting that the electron transfer pathway might indeed play a major role. Time–current curves were then examined to further validate the presence of electron transfer. The addition of PMS after the curve stabilized caused a slight change in current, which may be due to the effect of PMS adsorption on the working electrode surface. The addition of BPA after the curve stabilized again caused a dramatic drop in current, from 0.03 mA to below −0.03 mA, indicating that PMS and contaminants acted on the catalyst surface and underwent charge transfer, which is consistent with the electron transfer path previously reported in the literature. Based on these results, we can conclude that BPA was degraded by electron transfer, while ATZ was removed by the free radical pathway [25,50].

2.5. Selective Oxidation Mechanism

To investigate the differences in the degradation mechanisms of ATZ and BPA by the FeMIL-N-C/PMS system, we conducted DFT theoretical calculations on the structures of BPA and ATZ. The frontier orbital theory is commonly employed to assess the reactivity of organic molecules. A larger LUMO-HOMO energy gap ($E_{LUMO-HOMO}$) typically corresponds to a larger redox potential, and the redox potential determines whether the substance reacts easily or not. In simple terms, a larger LUMO-HOMO energy gap means that the molecule is reluctant to give electrons and is therefore less susceptible to degra-

dation, while a lower $E_{LUMO-HOMO}$ means that the molecule is more reactive and more willing to give electrons for a reaction. As shown in Figure 8, we calculated the LUMO and HOMO values for ATZ and BPA separately. For ATZ, $E_{LUMO-HOMO-ATZ}$ = 4.2 eV, while in BPA, $E_{LUMO-HOMO-BPA}$ = 2.67 eV. This leads to the different degradation mechanisms observed. For the FeMIL-N-C/PMS/BPA system, PMS can easily extract electrons from the BPA molecule and be degraded by electron transfer. This is in agreement with our experimental and theoretical calculations, as well as with some previous reports on electron transfer. Moreover, in the FeMIL-N-C/PMS/ATZ system, the higher redox potential of ATZ determines that it is not willing to give electrons, so PMS cannot easily extract electrons from it. On this basis, the degradation of ATZ can only be accomplished by the activation of FeMIL-N-C on PMS to generate free radicals with high oxidation potentials, and it depends heavily on the amount of PMS dosing, because only sufficient PMS dosing can ensure sufficient free radical generation to degrade ATZ.

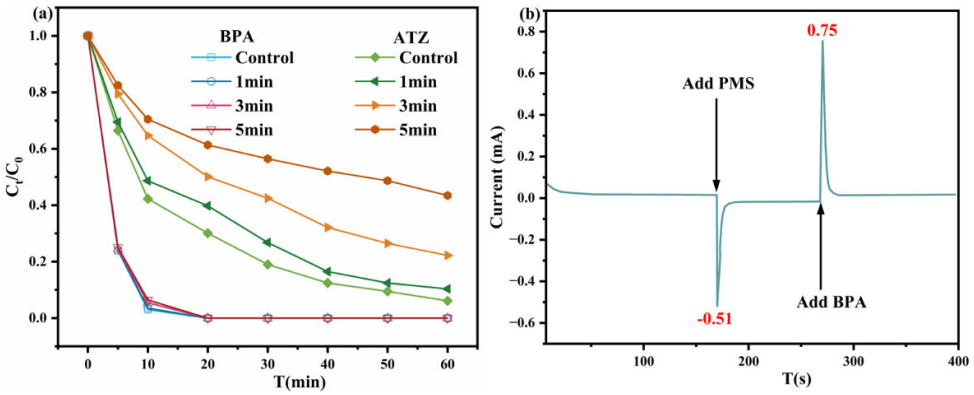

Figure 7. (**a**) Effect of pre-addition of PMS and FeMIL-N-C on BPA and ATZ, (**b**) time–current curves. Conditions: [catalyst] = 0.2 g·L^{-1}, [PMS] = 0.4 g·L^{-1}, [pollutants] = 20 mg·L^{-1}.

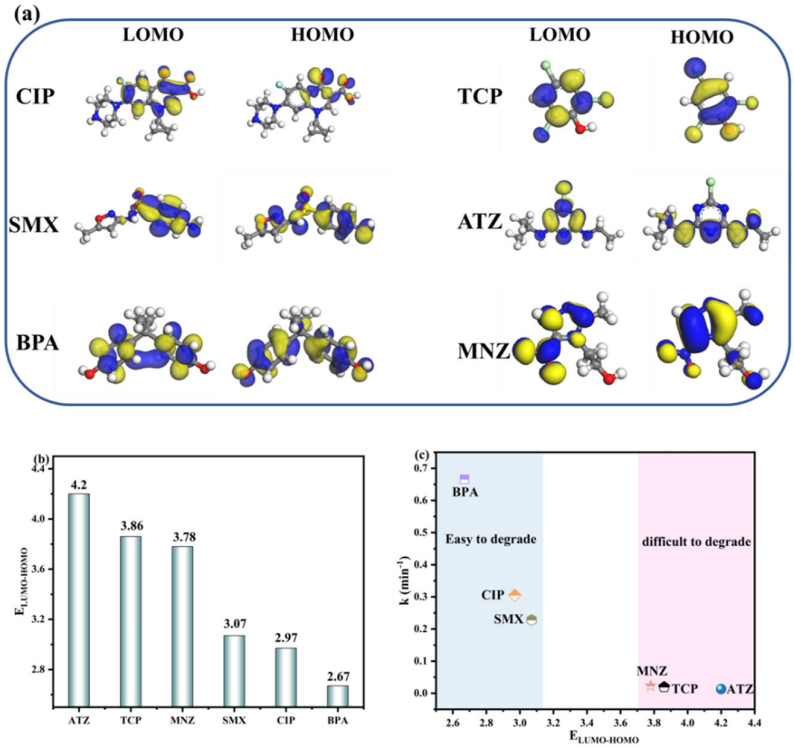

Figure 8. (**a**) LUMO-HOMO energy levels of different pollutants, (**b**) $E_{LUMO-HOMO}$ for different pollutants and (**c**) relationship between K-value and $E_{LUMO-HOMO}$.

In conclusion, BPA, with its lower redox potential, will be degraded via the electron transfer pathway (Figure 9). In this pathway, PMS first forms a complex intermediate by combining with Fe-Nx (Equation (1)). The complex intermediate then accepts electrons from PMS upon its addition to the solution, leading to the degradation of BPA (Equation (2)). On the other hand, ATZ, with its higher redox potential, is less susceptible to degradation through non-radical pathways due to its milder effects on its structure. Therefore, ATZ requires larger dosages of PMS to initiate degradation via the non-radical pathway (Equations (3) and (4))

$$Fe - N_x + HO - O - SO_3^- \rightarrow Fe - N_x \equiv HO - O - O - SO_3^- \quad (1)$$

$$Fe - N_x \equiv HO - O - SO_3^- + \text{pollutants} \rightarrow Fe - N_x + SO_4^{2-} + H^+ + \text{products} \quad (2)$$

$$2HSO_5^- + Fe{-}N_x \rightarrow 2SO_4^- \cdot + OH^- \quad (3)$$

$$2HSO_5^- + Fe{-}N_x \rightarrow SO_4^- \cdot + \cdot OH + SO_4^{2-} \quad (4)$$

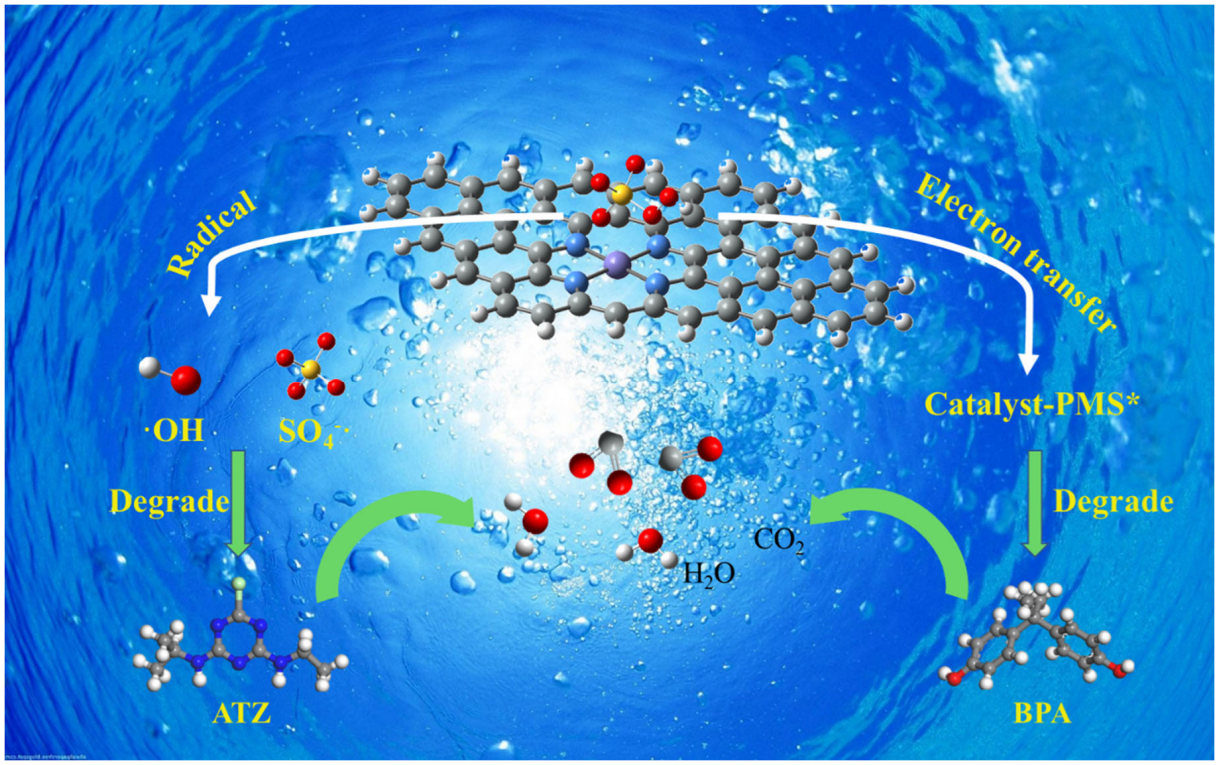

Figure 9. Degradation mechanism of FeMIL-N-C/PMS system for BPA and ATZ.

3. Experimental Section

3.1. Chemicals

The information on chemicals used in this study is listed in Text S1.

3.2. Synthesis of Catalyst

Fe (MIL) was synthesized according to the previous study protocol as described in Supplementary Information Text S2. Further, 0.793 g of Zn $(NO_3)_2 \cdot 6H_2O$ was added to 41.7 mL of methanol to form solution A; 0.824 g of 2-methylimidazole and 0.012 g of Hexadecyl trimethyl ammonium Bromide (CTAB) were added to 33.3 mL of methanol to form solution B. Then, solution A was poured into solution B and 10 mg of Fe(MIL) was

added at the same time. After continuous stirring for 5h at room temperature, the precursor Fe(MIL)-ZIF was obtained by centrifugation and was washed with methanol 3–5 times and dried at 60 °C;

Fe(MIL)-ZIF was placed in a quartz boat in a tube furnace and maintained at a heating rate of 5 °C/min to 900 °C under a nitrogen atmosphere for two hours, then washed with 0.1M sulfuric acid for 8 h and washed with deionized water to remove the acid and dried at 60 °C to obtain FeMIL-N-C.

3.3. Characterization

Specific details are provided in the Supplementary Information Text S3.

3.4. Experimental Procedure

The catalytic performances of FeMIL-N-C catalysts were evaluated by the adsorption and degradation of pollutants via the initial concentration of 20 mg/L. Typical experiments were conducted in a 250 mL bottle with 100 mL of the pollutant solution, which was placed in a shock incubator at 180 rpm at 25 °C. In a typical degradation experiment, a certain amount of PMS and FeMIL-N-C catalyst were added. The samples were taken at regular intervals and filtered through 0.22 μm filters, and then 1.0 mL of methanol (MeOH) was added immediately to stop the reaction and for further analysis. The adsorption experiment was the same as the above steps, except that PMS was added.

In the quenching experiments, the corresponding quenching agents FeMIL-N-C and PMS were added together to the contaminant solution, and the rest of the procedure was the same as above. Unless not otherwise specified, the quenching agent was PMS = 30:1 (mol:mol).

3.5. Analytical Methods

The analytical methods of high-performance liquid chromatography (HPLC), electronic chemical measurements, and electron paramagnetic resonance (EPR) are listed in Text S4 and Table S1. Kinetic analysis using the pseudo-first-order model is described in Text S5.

3.6. Calculation Methods

Information on the DFT calculations is listed in Text S6.

4. Conclusions

In this study, we developed a highly active Fe-N-C catalyst derived from MOFs using a pyrolysis protection strategy, and we assessed its catalytic performance by activating PMS for pollutant degradation. The presence of Fe-Nx sites in the FeMIL-N-C catalyst resulted in a remarkable 23-fold increase in catalytic activity compared to N-C. We conducted a comprehensive analysis of the degradation mechanism in the FeMIL-N-C/PMS system for different pollutants with varying electronic structures, namely BPA and ATZ. Our findings revealed that the degradation of ATZ predominantly occurred through the generation of free radicals and was significantly influenced by the dosage of PMS. Conversely, the degradation of BPA occurred via the electron transfer pathway due to its low LUMO-HOMO energy gap. In conclusion, this research provides a valuable approach for modulating the degradation pathway of pollutants, enabling the efficient removal of diverse contaminants. These findings contribute to the development of advanced oxidation processes with selective oxidation capabilities for treating complex water environments. Moreover, this work offers new insights into the degradation mechanisms of specific pollutants, enhancing our understanding of pollutant removal processes.

Supplementary Materials: The following supporting information can be downloaded at: https://www.mdpi.com/article/10.3390/catal13061021/s1, Figure S1: SEM of P-FeMIL; Figure S2: SEM of FeMIL-ZIF and EDX of FeMIL-ZIF; Figure S3: Effect of PMS dosage on ATZ degradation; Figure S4: Effect of PMS dosage on BPA degradation; Table S1: Elemental content by EDS; Text S1: Chemicals; Text S2: Synthesis of FeMIL; Text S3: Characterization; Text S4: Analytical Methods; Text S5: Calculation of reaction kinetics, Text S6: Method of theoretical calculation.

Author Contributions: C.Z.: Conceptualization, methodology, data curation, formal analysis, writing—original draft, writing—review and editing. Y.W.: Formal analysis, investigation, writing—review and editing. J.W.: Supervision, investigation, funding acquisition. Z.Y.: Investigation, writing—review and editing. All authors have read and agreed to the published version of the manuscript.

Funding: This work was funded by Guangdong Basic and Applied Basic Research Foundation (2023A1515011186), the National Key Research and Development Project (No. 2018YFE0110400), the National Natural Science Foundation of China (No. 22278156 and No. 21978102), the Guangdong Special Program (No. 2021JC060580), and the Foshan Science and Technology Innovation Project of Guangdong Province (No. 2130218003140).

Data Availability Statement: Not applicable.

Conflicts of Interest: The authors declare no conflict of interest.

References

1. Wang, J.; Chu, L.; Wojnarovits, L.; Takacs, E. Occurrence and fate of antibiotics, antibiotic resistant genes (ARGs) and antibiotic resistant bacteria (ARB) in municipal wastewater treatment plant: An overview. *Sci. Total Environ.* **2020**, *744*, 140997. [CrossRef]
2. Du, H.; Yang, Z.; Tian, Z.; Huang, M.; Yang, W.; Zhang, L.; Li, A. Enhanced removal of trace antibiotics from turbid water in the coexistence of natural organic matters using phenylalanine-modified-chitosan flocculants: Effect of flocculants' molecular architectures. *Chem. Eng. J.* **2018**, *333*, 310–319. [CrossRef]
3. Rozas, O.; Vidal, C.; Baeza, C.; Jardim, W.F.; Rossner, A.; Mansilla, H.D. Organic micropollutants (OMPs) in natural waters: Oxidation by UV/H2O2 treatment and toxicity assessment. *Water Res.* **2016**, *98*, 109–118. [CrossRef] [PubMed]
4. Wang, Y.; Xiao, T.; Zuo, S.; Wan, J.; Yan, Z.; Zhu, B.; Zhang, X. Exploring degradation properties and mechanisms of emerging contaminants via enhanced directional electron transfer by polarized electric fields regulation in Fe-N_4-Cx. *J. Hazard. Mater.* **2023**, *446*, 130698. [CrossRef]
5. Du, Z.; Qin, J.; Zhang, K.; Jia, L.; Tian, K.; Zhang, J.; Xie, H. N-doped carbon nanosheets supported-single Fe atom for p-nitrophenol degradation via peroxymonosulfate activation. *Appl. Surf. Sci.* **2022**, *591*, 153124. [CrossRef]
6. Xu, X.; Zhan, F.; Pan, J.; Zhou, L.; Su, L.; Cen, W.; Li, W.; Tian, C. Engineering single-atom Fe-Pyridine N_4 sites to boost peroxymonosulfate activation for antibiotic degradation in a wide pH range. *Chemosphere* **2022**, *294*, 133735. [CrossRef]
7. Lu, D.L.; Chen, Z.; Yang, Q.D.; Han, S. Efficient novel FeOCl/C with high singlet oxygen generation for TCH degradation. *Chem. Phys. Lett.* **2022**, *800*, 139664. [CrossRef]
8. Xiao, T.; Wang, Y.; Wan, J.; Ma, Y.; Yan, Z.; Huang, S.; Zeng, C. Fe-N-C catalyst with Fe-N-X sites anchored nano carboncubes derived from Fe-Zn-MOFs activate peroxymonosulfate for high-effective degradation of ciprofloxacin: Thermal activation and catalytic mechanism. *J. Hazard. Mater.* **2022**, *424*, 127380. [CrossRef] [PubMed]
9. Olmez-Hanci, T.; Arslan-Alaton, I. Comparison of sulfate and hydroxyl radical based advanced oxidation of phenol. *Chem. Eng. J.* **2013**, *224*, 10–16. [CrossRef]
10. Li, H.X.; Wan, J.Q.; Ma, Y.W.; Wang, Y. Reaction pathway and oxidation mechanisms of dibutyl phthalate by persulfate activated with zero-valent iron. *Sci. Total Environ.* **2016**, *562*, 889–897. [CrossRef] [PubMed]
11. Rastogi, A.; Ai-Abed, S.R.; Dionysiou, D.D. Sulfate radical-based ferrous-peroxymonosulfate oxidative system for PCBs degradation in aqueous and sediment systems. *Appl. Catal. B-Environ.* **2009**, *85*, 171–179. [CrossRef]
12. Waclawek, S.; Lutze, H.V.; Grubel, K.; Padil, V.V.T.; Cernik, M.; Dionysiou, D.D. Chemistry of persulfates in water and wastewater treatment: A review. *Chem. Eng. J.* **2017**, *330*, 44–62. [CrossRef]
13. Yin, R.; Guo, W.; Wang, H.; Du, J.; Wu, Q.; Chang, J.-S.; Ren, N. Singlet oxygen-dominated peroxydisulfate activation by sludge-derived biochar for sulfamethoxazole degradation through a nonradical oxidation pathway: Performance and mechanism. *Chem. Eng. J.* **2019**, *357*, 589–599. [CrossRef]
14. Rastogi, A.; Al-Abed, S.R.; Dionysiou, D.D. Effect of inorganic, synthetic and naturally occurring chelating agents on Fe(II) mediated advanced oxidation of chlorophenols. *Water Res.* **2009**, *43*, 684–694. [CrossRef]
15. Zhang, R.C.; Yang, Y.K.; Huang, C.H.; Zhao, L.; Sun, P.Z. Kinetics and modeling of sulfonamide antibiotic degradation in wastewater and human urine by UV/H_2O_2 and UV/PDS. *Water Res.* **2016**, *103*, 283–292. [CrossRef] [PubMed]
16. Li, B.Z.; Li, L.; Lin, K.F.; Zhang, W.; Lu, S.G.; Luo, Q.S. Removal of 1,1,1-trichloroethane from aqueous solution by a sono-activated persulfate process. *Ultrason. Sonochemistry* **2013**, *20*, 855–863. [CrossRef]

17. Ji, Y.F.; Fan, Y.; Liu, K.; Kong, D.Y.; Lu, J.H. Thermo activated persulfate oxidation of antibiotic sulfamethoxazole and structurally related compounds. *Water Res.* **2015**, *87*, 1–9. [CrossRef] [PubMed]
18. Fan, Y.; Ji, Y.F.; Kong, D.Y.; Lu, J.H.; Zhou, Q.S. Kinetic and mechanistic investigations of the degradation of sulfamethazine in heat-activated persulfate oxidation process. *J. Hazard. Mater.* **2015**, *300*, 39–47. [CrossRef] [PubMed]
19. Duan, X.G.; Sun, H.Q.; Shao, Z.P.; Wang, S.B. Nonradical reactions in environmental remediation processes: Uncertainty and challenges. *Appl. Catal. B-Environ.* **2018**, *224*, 973–982. [CrossRef]
20. Duan, X.G.; Ao, Z.M.; Zhou, L.; Sun, H.Q.; Wang, G.X.; Wang, S.B. Occurrence of radical and nonradical pathways from carbocatalysts for aqueous and nonaqueous catalytic oxidation. *Appl. Catal. B-Environ.* **2016**, *188*, 98–105. [CrossRef]
21. Shang, Y.N.; Xu, X.; Gao, B.Y.; Wang, S.B.; Duan, X.G. Single-atom catalysis in advanced oxidation processes for environmental remediation. *Chem. Soc. Rev.* **2021**, *50*, 5281–5322. [CrossRef]
22. Huang, L.-Z.; Wei, X.; Gao, E.; Zhang, C.; Hu, X.-M.; Chen, Y.; Liu, Z.; Finck, N.; Luetzenkirchen, J.; Dionysiou, D.D. Single Fe atoms confined in two-dimensional MoS2 for sulfite activation: A biomimetic approach towards efficient radical generation. *Appl. Catal. B-Environ.* **2020**, *268*, 118459. [CrossRef]
23. Qian, K.; Chen, H.; Li, W.; Ao, Z.; Wu, Y.-N.; Guan, X. Single-Atom Fe Catalyst Outperforms Its Homogeneous Counterpart for Activating Peroxymonosulfate to Achieve Effective Degradation of Organic Contaminants. *Environ. Sci. Technol.* **2021**, *55*, 7034–7043. [CrossRef] [PubMed]
24. Li, Y.; Yang, T.; Qiu, S.; Lin, W.; Yan, J.; Fan, S.; Zhou, Q. Uniform N-coordinated single-atomic iron sites dispersed in porous carbon framework to activate PMS for efficient BPA degradation via high-valent iron-oxo species. *Chem. Eng. J.* **2020**, *389*, 124382. [CrossRef]
25. Oh, W.-D.; Dong, Z.; Lim, T.-T. Generation of sulfate radical through heterogeneous catalysis for organic contaminants removal: Current development, challenges and prospects. *Appl. Catal. B Environ.* **2016**, *194*, 169–201. [CrossRef]
26. Xiao, M.; Xing, Z.; Jin, Z.; Liu, C.; Ge, J.; Zhu, J.; Wang, Y.; Zhao, X.; Chen, Z. Preferentially Engineering FeN4 Edge Sites onto Graphitic Nanosheets for Highly Active and Durable Oxygen Electrocatalysis in Rechargeable Zn–Air Batteries. *Adv. Mater.* **2020**, *32*, 2004900. [CrossRef] [PubMed]
27. Nabae, Y.; Nagata, S.; Kusaba, K.; Aoki, T.; Hayakawa, T.; Tanida, H.; Imai, H.; Hori, K.; Yamamoto, Y.; Arai, S.; et al. Magnetic purification of non-precious metal fuel cell catalysts for obtaining atomically dispersed Fe centers. *Catal. Sci. Technol.* **2020**, *10*, 493–501. [CrossRef]
28. Chung, H.T.; Cullen, D.A.; Higgins, D.; Sneed, B.T.; Holby, E.F.; More, K.L.; Zelenay, P. Direct atomic-level insight into the active sites of a high-performance PGM-free ORR catalyst. *Science* **2017**, *357*, 479–483. [CrossRef]
29. Huang, Z.K.; Yu, H.J.; Wang, L.; Wang, M.Y.; Liu, X.W.; Shen, D.; Shen, S.D.; Ren, S.N.; Lin, T.F.; Lei, S.Y. Ferrocene doped ZIF-8 derived Fe-N-C single atom catalyst to active peroxymonosulfate for removal of bisphenol A. *Sep. Purif. Technol.* **2023**, *305*, 122402. [CrossRef]
30. Miao, J.; Zhu, Y.; Lang, J.Y.; Zhang, J.Z.; Cheng, S.X.; Zhou, B.X.; Zhang, L.Z.; Alvarez, P.J.J.; Long, M.C. Spin-State-Dependent Peroxymonosulfate Activation of Single-Atom M-N Moieties via a Radical-Free Pathway. *ACS Catal.* **2021**, *11*, 9569–9577. [CrossRef]
31. Zhu, Y.; Zhu, R.; Xi, Y.; Zhu, J.; Zhu, G.; He, H. Strategies for enhancing the heterogeneous Fenton catalytic reactivity: A review. *Appl. Catal. B Environ.* **2019**, *255*, 117739. [CrossRef]
32. Gao, Y.W.; Zhu, Y.; Li, T.; Chen, Z.H.; Jiang, Q.K.; Zhao, Z.Y.; Liang, X.Y.; Hu, C. Unraveling the High-Activity Origin of Single-Atom Iron Catalysts for Organic Pollutant Oxidation via Peroxymonosulfate Activation. *Environ. Sci. Technol.* **2021**, *55*, 8318–8328. [CrossRef] [PubMed]
33. Ren, W.; Xiong, L.L.; Nie, G.; Zhang, H.; Duan, X.G.; Wang, S.B. Insights into the Electron-Transfer Regime of Peroxydisulfate Activation on Carbon Nanotubes: The Role of Oxygen Functional Groups. *Environ. Sci. Technol.* **2020**, *54*, 1267–1275. [CrossRef] [PubMed]
34. Ren, W.; Nie, G.; Zhou, P.; Zhang, H.; Duan, X.G.; Wang, S.B. The Intrinsic Nature of Persulfate Activation and N-Doping in Carbocatalysis. *Environ. Sci. Technol.* **2020**, *54*, 6438–6447. [CrossRef]
35. Jiao, D.X.; Liu, Y.J.; Cai, Q.H.; Zhao, J.X. Coordination tunes the activity and selectivity of the nitrogen reduction reaction on single-atom iron catalysts: A computational study. *J. Mater. Chem. A* **2021**, *9*, 1240–1251. [CrossRef]
36. Dang, S.; Zhu, Q.-L.; Xu, Q. Nanomaterials derived from metal-organic frameworks. *Nat. Rev. Mater.* **2018**, *3*, 17075. [CrossRef]
37. Wu, W.; Lei, W.; Wang, L.; Wang, S.; Zhang, H. Preparation of Single Atom Catalysts. *Prog. Chem.* **2020**, *32*, 23–32. [CrossRef]
38. Li, X.; Wan, J.; Wang, Y.; Chi, H.; Yan, Z.; Ding, S. Selective removal and persulfate catalytic decomposition of diethyl phthalate from contaminated water on modified MIL100 through surface molecular imprinting. *Chemosphere* **2020**, *240*, 124875. [CrossRef]
39. Wang, L.; Wan, X.; Liu, S.Y.; Xu, L.; Shui, J.L. Fe-N-C catalysts for PEMFC: Progress towards the commercial application under DOE reference. *J. Energy Chem.* **2019**, *39*, 77–87. [CrossRef]
40. Jiang, Z.; Xie, Y.; Li, C.; Zheng, J.; Si, M.; Xiao, R.; Liao, Q.; Yang, W. Non-radical dominated catalytic degradation of chlorophenol by a structure-tailored catalyst of high nitrogen doping carbon matrix with nano-CuO. *J. Environ. Chem. Eng.* **2022**, *10*, 107559. [CrossRef]
41. He, J.; Wan, Y.; Zhou, W. ZIF-8 derived Fe-N coordination moieties anchored carbon nanocubes for efficient peroxymonosulfate activation via non-radical pathways: Role of FeNx sites. *J. Hazard. Mater.* **2021**, *405*, 124199. [CrossRef] [PubMed]
42. Han, A.; Wang, B.; Kumar, A.; Qin, Y.; Jin, J.; Wang, X.; Yang, C.; Dong, B.; Jia, Y.; Liu, J.; et al. Recent Advances for MOF-Derived Carbon-Supported Single-Atom Catalysts. *Small Methods* **2019**, *3*, 1800471. [CrossRef]

43. An, S.F.; Zhang, G.H.; Wang, T.W.; Zhan, W.N.; Li, K.Y.; Song, C.S.; Miller, J.T.; Miao, S.; Wang, J.H.; Guo, X.W. High-Density Ultra-small Clusters and Single-Atom Fe Sites Embedded in Graphitic Carbon Nitride (g-C_3N_4) for Highly Efficient Catalytic Advanced Oxidation Processes. *ACS Nano* **2018**, *12*, 9441–9450. [CrossRef]
44. Pu, M.J.; Niu, J.F.; Brusseau, M.L.; Sun, Y.L.; Zhou, C.Z.; Deng, S.; Wan, J.Q. Ferrous metal-organic frameworks with strong electron-donating properties for persulfate activation to effectively degrade aqueous sulfamethoxazole. *Chem. Eng. J.* **2020**, *394*, 125044. [CrossRef]
45. Wang, F.L.; Wang, Y.F.; Li, Y.Y.; Cui, X.H.; Zhang, Q.X.; Xie, Z.J.; Liu, H.J.; Feng, Y.P.; Lv, W.Y.; Liu, G.G. The facile synthesis of a single atom-dispersed silver-modified ultrathin g-C_3N_4 hybrid for the enhanced visible-light photocatalytic degradation of sulfamethazine with peroxymonosulfate. *Dalton Trans.* **2018**, *47*, 6924–6933. [CrossRef]
46. Ao, X.W.; Liu, W.J. Degradation of sulfamethoxazole by medium pressure UV and oxidants: Peroxymonosulfate, persulfate, and hydrogen peroxide. *Chem. Eng. J.* **2017**, *313*, 629–637. [CrossRef]
47. Du, N.; Liu, Y.; Li, Q.; Miao, W.; Wang, D.; Mao, S. Peroxydisulfate activation by atomically-dispersed Fe-Nx on N-doped carbon: Mechanism of singlet oxygen evolution for nonradical degradation of aqueous contaminants. *Chem. Eng. J.* **2021**, *413*, 127545. [CrossRef]
48. Li, H.; Wan, J.; Ma, Y.; Huang, M.; Wang, Y.; Chen, Y. New insights into the role of zero-valent iron surface oxidation layers in persulfate oxidation of dibutyl phthalate solutions. *Chem. Eng. J.* **2014**, *250*, 137–147. [CrossRef]
49. Wang, Y.; Hu, F.-L.; Mi, Y.; Yan, C.; Zhao, S. Single-metal-atom catalysts: An emerging platform for electrocatalytic oxygen reduction. *Chem. Eng. J.* **2021**, *406*, 127135. [CrossRef]
50. Yang, J.; Zeng, D.; Li, J.; Dong, L.; Ong, W.-J.; He, Y. A highly efficient Fenton-like catalyst based on isolated diatomic Fe-Co anchored on N-doped porous carbon. *Chem. Eng. J.* **2021**, *404*, 126376. [CrossRef]